Student symposium, session I, May 26, Tuesday

SL1

EFFECT OF COLD-ROLLING FOLLOWED BY SHOT PEENING ON MICROSTRUCTURAL PARAMETERS IN EN 1.4470 DUPLEX STEEL

M. Rušin, J. Čapek, K. Trojan

Department of Solid State Engineering, Faculty of Nuclear Sciences and Physical Engineering, Czech Technical University in Prague
rusinma3@cvut.cz

Duplex stainless steels (DSS) combine a microstructure of ferrite (-Fe) with austenite (-Fe) in roughly 1:1 ratio. Chemical composition and content of alloying elements determine final properties, creating many types and grades of DSS. Most of DSS surpass austenitic stainless steels in their physical and chemical properties. Therefore, DSS are widely used in civil engineering, aviation and automotive industries, and even food storage. [1] Shot peening process (SP) is a cold working process known for its enhancement of service life by introducing compressive residual stresses into material. By bombarding the surface with small spherical media, plastic deformation is induced, altering real structure in subsurface regions. [2] Although rolling is nowadays a standard step in production and processing of steel products, its combination with SP introduces new possibilities for real structure modifications. Prior research of SP has shown that effects of rolling persist in the material and are not fully supressed even after SP. The effect of rolling was studied using X-ray diffraction techniques and the depth distributions of crystallite sizes and microstrains are described.

Three sheets of EN 1.4470 DSS with chemical composition (in wt.%): 22.2 Cr, 5.5 Ni, 3.28 Mo, 0.41 Si, 0.13 Cu, 0.09 Al, 0.034 V, 0.006 Nb, 0.005 Sn and bal. Fe, were cut and ground to different thicknesses. After stress relieve annealing, they were cold rolled to final thickness of 1.5 mm, achieving thickness reductions of 10, 40, and 50 % compared to original size after rolling. According to that, samples are designated as R10, R40 and R50 respectively. After another stress relieve annealing, the SP treatment was carried out in a self-made machine using quenched steel shots. Almen intensity 1.90 ± 0.08 mmA was achieved, measured by the arc height of A type Almen strip (strip thickness 1.295 ± 0.025 mm) [3]. The SP direction was the same as the rolling direction (RD). Due to limited penetration depth of X-rays, layers of the material were gradually removed after each measurement, with aim to analyse the gradients of aforementioned parameters. *PROTO Electrolytic polisher 8818-V3* with A type electrolyte was used for electrolytic polishing. A micrometre screw gauge was used to determine the removed layer thickness by calculating the difference between thicknesses before and after polishing.

For obtaining the XRD patterns the *Empyrean PANanalytical* diffractometer in Bragg-Brentano geometry was used. Irradiated volume was defined by the experimental geometry, effective penetration depth of X-rays and the pinhole size (0.5 × 1 mm). Obtained patterns were used for Rietveld analysis using *MStruct* software. Crystallite sizes and microstrains were calculated from diffraction line broadening as described on the official website [4]. It has to be noted that -Fe is a metastable phase, and martensitic phase transformation is possible. Strain-induced martensite can by formed both by rolling and SP. In low carbon steels,

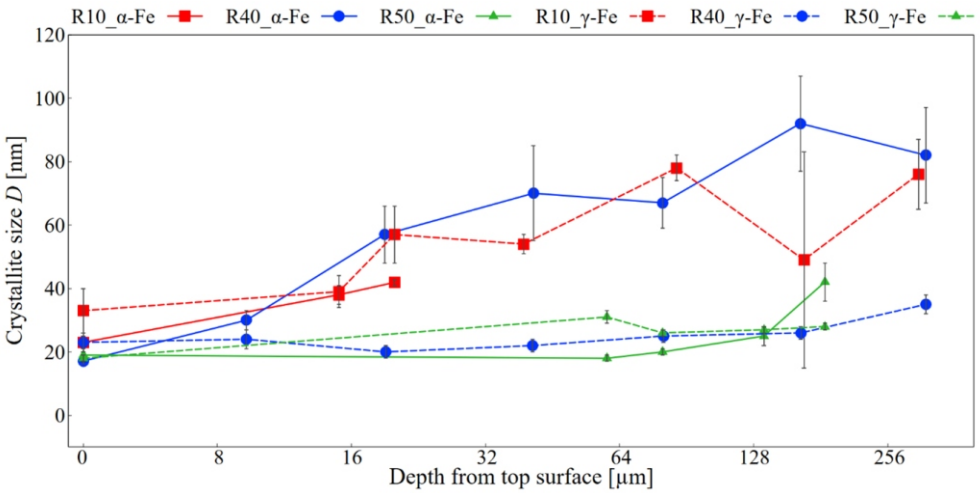

Figure 1. The depth distributions of the crystallite size *D*.

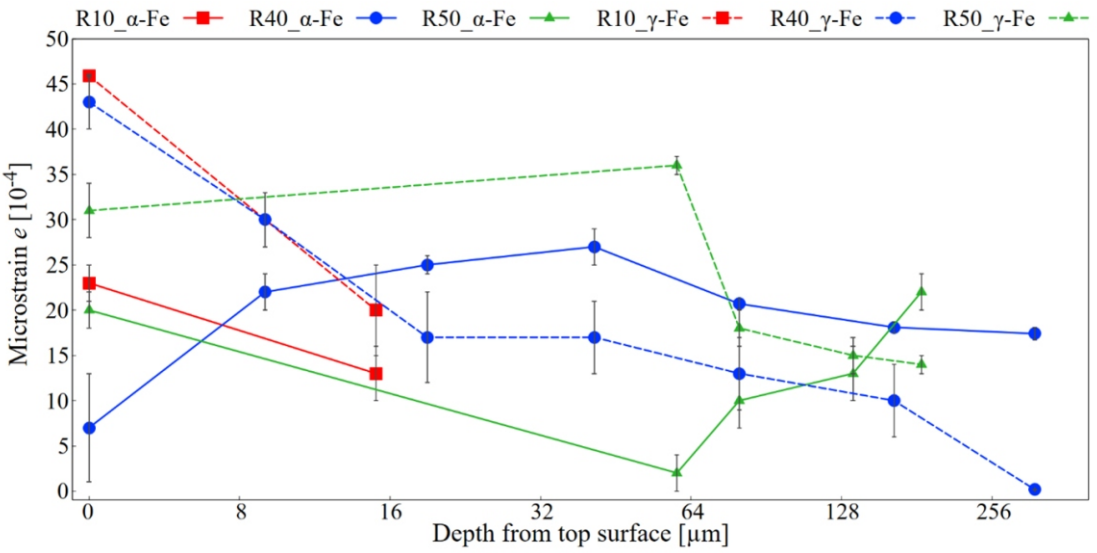

Figure 2. The depth distributions of the microstrain $e \times 10^{-4}$.

the tetragonality of martensite lattice is small . Therefore, these two phases cannot be directly distinguished by XRD techniques. Symbol -Fe therefore represents both ferrite and martensite.

Results for crystallite sizes are shown in Fig. 1. As could be expected, SP process caused their reduction in near surface regions. The effect is however pronounced only to certain depth. Two effects of previous rolling can be seen, when comparing the samples to one another. Firstly, samples with lower thickness reduction have larger crystallites, due to lower deformation, both in bulk and near surface region. From this trend deviates only the -Fe phase of R10 sample. After first two measured depths, sudden drop in its crystallite size was observed. This behaviour is related to the effect of preferred orientation in the material, which can alter the intensity of individual diffraction lines. Affected diffraction pattern is insufficient for an accurate determination of crystallite size. Inaccurate values were therefore omitted in Fig. 1. The explained trend in crystallite size due to different amount of rolling is rather expected. The second effect is of more interest. It can be seen in sample R50 and -Fe of sample R40, that the change in crystallite sizes between near surface regions, surely affected by SP, and bulk regions is less pronounced. This phenomenon can be attributed to work hardening. Samples rolled to higher thickness reductions are more deformed, therefore exhibiting harder surface. In contrast, surface of samples rolled to lower reduction is easily deformed by the impact of the SP medium. In DSS, the work-hardening rate of -Fe is higher than of -Fe [5], explaining the difference between phases of R40 sample. However, the same effect in R50 sample was not observed for reasons that remain to be identified. From the overall results, it cannot be stated which phase of DSS was more affected. It should be emphasised again, that resulting values for -Fe are influenced by the crystallite size of the stress-induced martensite. These crystallites originally correspond to -Fe that underwent a phase transformation. However, the martensitic crystallites do not necessarily deform in the same manner as the -Fe crystallites.

Microstrains were analysed together with crystallite sizes and are shown in Fig. 2. They are closely related to size of crystallites and can be seen as complementary results. Near surface regions are affected by SP, causing higher microstrains. Similarly to crystallite size, the change between surface and bulk region is less pronounced for higher reductions in -Fe phase. Results for -Fe are related to crystallite sizes. In larger crystallites, lower microstrains can be expected, which was also observed. For reasons described before, reliable results for R10 sample could not be obtained. Apart from this sample, the effect of rolling remains present in the samples despite their annealing. The reason is the mutual interaction between the crystallites of both phases during deformation. Both phases are deformed differently during rolling. For example, at small deformations, the work-hardening rate of -Fe is relatively high, however, once the thickness reduction exceeds 15%, the deformation becomes more concentrated in -Fe, which has higher stacking fault energy [5]. This might be the explanation behind sudden increase in microstrain of R50 -Fe phase in bulk region. The effect is not observed for R40 sample, due to its larger crystallites.

Generally, it was observed that rolling affects the further change of microstructural parameters caused by SP. Higher reduction in thickness introduces more strain hardening, which constrains further crystallite size reduction. With smaller crystallites, microstrain values tend to be higher. Unfortunately, R10 sample was highly affected by preferred orientation and to fully understand the effect of rolling on microstructural parameters, further research is needed.

1. TMR Stainless, Practical Guidelines for the Fabrication of Duplex Stainless Steel, London: IMOA, 2014.
2. J. Champaine, Shot Peening Overview, *The Shot Peener*, 2001.

3. M. Neslušan, P. Minárik, R. Čep, J. Uríček, K. Trojan, N. Ganev, L. Trško, Barkhausen noise emission of AISI 304 stainless steel originating from strain induced martensite by shot peening, *Journal of Materials Research and Technology*, **20**, (2022), 748-762.

4. Z. Matej et al., "MStruct - software for MicroStructure analysis by powder diffraction" Online. Available at: https://www.xray.cz/mstruct/mstruct-basic-ex.html. [accessed 2026-04-16].

5. W. Reick, M. Pohl, A. F. Padhila, Determination of stacking fault energy of austenite in a duplex stainless steel, Materials technology, **6**, (1996), 253-256.

This work was supported by the Grant Agency of the Czech Technical University in Prague, grant No. SGS25/168/OHK4/3T/14. We would also like to acknowledge prof. Dr. Ing. Miroslav Neslušan from University of Žilina for carrying out the SP process.

SL2

THE INFLUENCE OF ADDITIVE MANUFACTURING AND HEAT TREATMENT ON THE STRUCTURE PARAMETERS OF AlSi10Mg ALLOY

M. Endrych[1], K. Trojan[1], J. Čapek[1], R. Halama[2]

[1]Department of Solid State Engineering, Faculty of Nuclear Sciences and Physical Engineering, Czech Technical University in Prague; Trojanova 13, 120 00 Prague, Czech Republic

[2]VSB - Technical University of Ostrava; 17. listopadu 2172/15, 708 00 Ostrava - Poruba, Czech Republic

endrymar@cvut.cz

Selective laser melting (SLM) technology, one of the additive manufacturing methods, is a process of producing components from metal powder using laser melting. This manufacturing technology is able to meet demanding requirements for complex shapes, as well as shorten production times [1]. Due to high temperature gradients during non-uniform melting and cooling, the microstructure is very fine, anisotropic, and can exhibit elevated residual stress levels [2]. Important structural parameters that influence the real structure of materials include residual stresses and crystallographic preferred orientation (texture) [3]. An effective method for relieving elevated RS is the post-processing of as-built materials via heat treatment. Depending on the required mechanical properties, various heat treatment processes may be considered. These include solution and ageing treatments, direct ageing treatments or annealing over a wide range of temperatures and durations [4]. Annealing at intermediate temperatures can be optimized to relax RS, choose the desired level of strength, or increase ductility for Al-Si alloys [4].

This study investigates residual stresses and crystallographic preferred orientation of AlSi10Mg samples prepared by SLM technology. X-ray diffraction methods were employed using *Empyrean PANalytical* diffractometer. The aim is to examine the effect of heat treatment on these structure parameters and description with respect to various inclination angles relative to the normal of the building platform. For this, six cylindrical samples with a diameter of 10 mm and different inclination angles (0°, 10°, 20°, 30°, 40°, and 90°) were prepared. The axial direction is defined by the axis of the cylinder. After measurements on as-built samples, the samples were subsequently annealed at 300 °C for 4 h in argon atmosphere.

Macroscopic residual stresses in the axial and tangential directions for samples with various inclination angles were determined using the $\sin^2$ method. The {*311*} diffraction line of the aluminium phase was used. Results for as-built samples are shown in Fig. 1a and for annealed samples in Fig. 1b. Tensile residual stresses up to 60 MPa

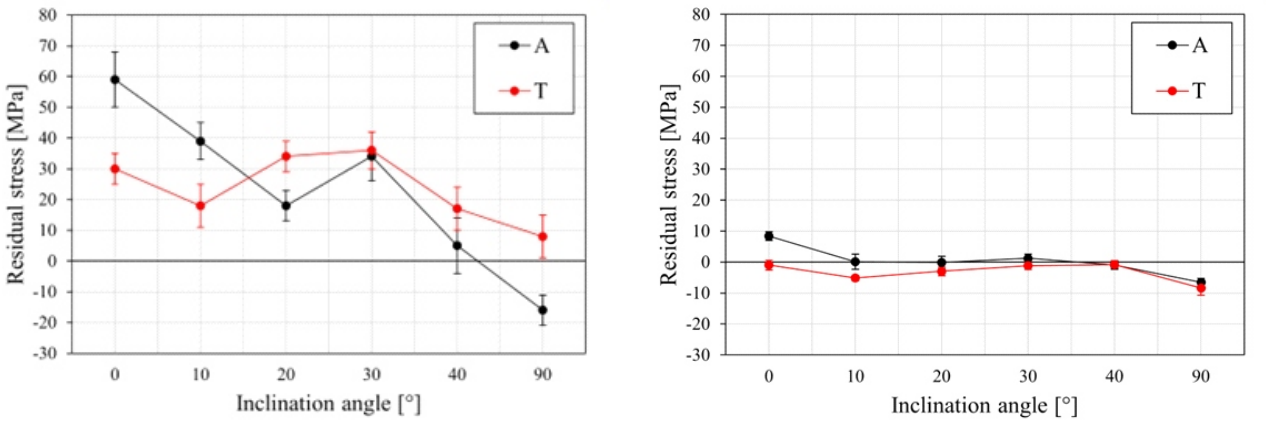

a) as-built samples

b) annealed samples

Figure 1. Residual stresses in the axial (A) and tangential (T) directions.

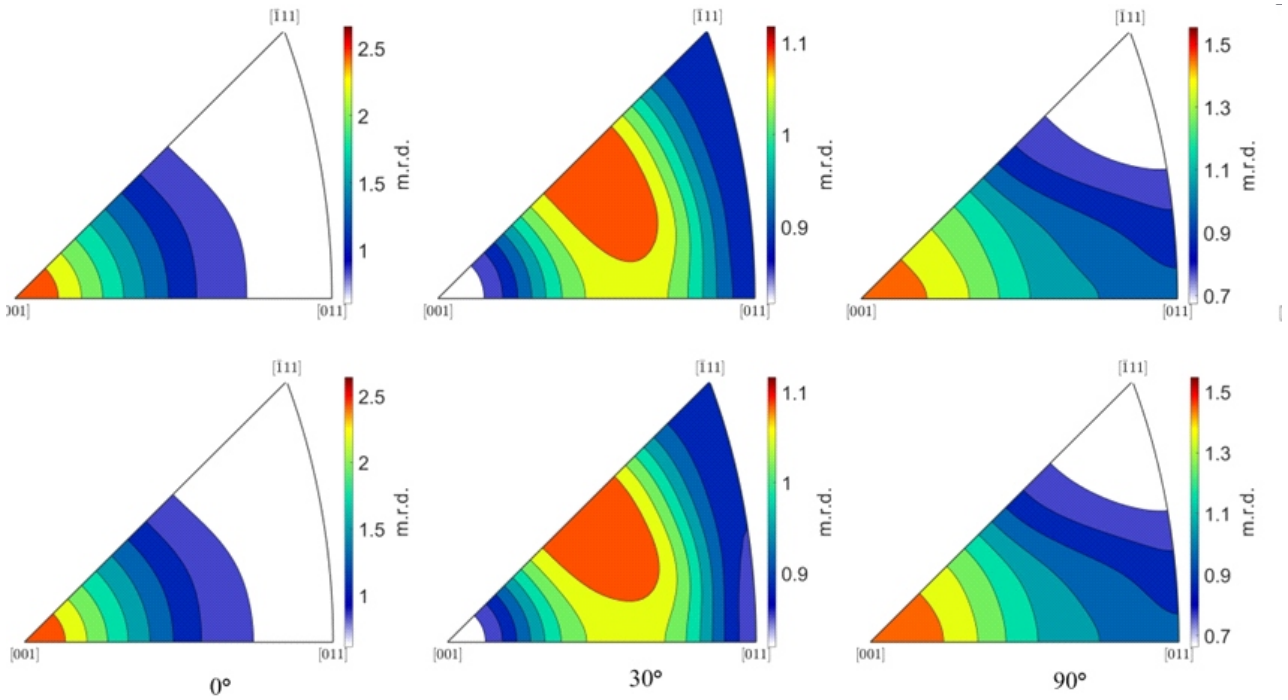

Figure 2. Inverse pole figures for axial direction of samples with inclination angles 0°, 30°, and 90° for as-built (up) and annealed (down) samples. The colour scale is in multiples of a random distribution (m.r.d.).

are observed in the as-built samples. Annealing at 300 °C resulted in a significant decrease in residual stresses.

Texture was analysed by inverse pole figures, which were calculated from experimental pole figures obtained by analysis of {*040*}, {*131*}, and {*222*} diffraction lines. For this *MATLAB* toolbox *MTEX* [5] was used. Inverse pole figures for the axial direction in three selected samples with inclination angles of 0°, 30°, and 90°, in both as-built and annealed conditions, are shown in Fig. 2. In the sample with an inclination of 0°, a strong *<100>* fibre texture is visible in the axial direction, which here corresponds to the direction of printing. It was found that *100* fibre texture is directly linked to the printing direction in all six examined samples. Annealing at 300 °C resulted in nearly no change in texture compared to the as-built samples.

1. J. Zhang, Y. Jung, *Additive manufacturing: Materials, processes, quantifications and applications*, Butterworth-Heinemann, Elsevier, 2018.
2. Q. Yan, B. Song, Y. Shi, *Journal of Materials Science & Technology*, **41**, (2020), 199-208.
3. I. Kraus, N. Ganev, *Technické aplikace difrakční analýzy*, Vydavatelství ČVUT, 2004.
4. J. Fiocchi, A. Tuissi, C.A. Biffi, *Materials & Design*, **204**, (2021), 109651.
5. F. Bachmann, R. Hielscher, H. Schaeben, *Solid State Phenomena*, **160**, (2010), 63-68.

This work was supported by the Grant Agency of the Czech Technical University in Prague, grant No. SGS25/168/OHK4/3T/14.

SL3

MULTISCALE STUDY OF THE INTERMITTENCY OF PLASTIC DEFORMATION BY MICROCT AND ACOUSTIC EMISSION METHOD IN Al-2Mg ALLOY FOAM

Ubaid Ahmed[1,2], Daniel Šimek[1], Michal Knapek[2], Tomáš Tayari[2], Lukáš Horák[2]

[1]FZU, Institute of Physics of the Czech Academy of Sciences, Na Slovance 2, Prague 8, 182 21, Czech Republic
[2]Matfyz Charles University, Prague, Czech Republic

In this work, we investigate the multiscale characteristics of deformation intermittency in an Al–2Mg alloy foam using a combination of in situ X-ray micro-computed tomography (microCT), digital volume correlation (DVC), and acoustic emission (AE) monitoring during quasi-static loading. The global mechanical response exhibits pronounced serrations in the force–elongation curve, indicating discrete deformation events. AE measurements reveal burst-type acoustic activity occurring during these load fluctuations. Tomographic scans were acquired after each successive load drop, enabling stepwise characterization of the evolving internal structure.

Three-dimensional displacement and strain fields were computed from successive tomographic volumes using DVC. The full-field analysis reveals heterogeneous strain distributions with localized regions of elevated axial strain

within the foam structure. These regions are spatially associated with structural rearrangements and local collapse of cell walls observed in the reconstructed volumes.

Comparison between DVC-derived global strain and externally measured strain highlights the influence of system compliance on the apparent macroscopic response, emphasizing the importance of internal strain measurements.

The combined microCT–DVC–AE methodology provides a framework for correlating macroscopic load fluctuations, internal strain heterogeneity, and acoustic activity, contributing to a better understanding of intermittent deformation in cellular metals.

SL4

CRYSTAL STRUCTURE AND MAGNETISM OF A NOVEL PYROCHLORE-TYPE QUATERNARY IRIDATE

F. Hájek[1], D. Staško[1], K. Vlášková[1], J. Kaštil[2], M. Henriques[2], M. Klicpera[1]

[1]Charles University, Faculty of Mathematics and Physics, Department of Condensed Matter Physics, Ke Karlovu 5, 121 16 Prague 2, Czech Republic

[2]Institute of Physics of the Czech Academy of Sciences, Na Slovance 2, 182 21 Prague 8, Czech Republic

filip.hajek@matfyz.cuni.cz

In recent years, oxides incorporating Ir^{4+} have attracted considerable attention of the condensed matter community, as strong spin orbit coupling and intermediary electron correlations of the 5d valence orbital lead to various exotic topological and magnetic properties [1]. Ir^{4+}, with configuration $5d^5$, is typically found in an octahedral ligand field, leading to a spin-orbit coupled effective $j_{eff} = 1/2$ orbital state [1, 2]. Quintessential examples of such iridates are Sr_2IrO_4 [3] and $A_2Ir_2O_7$ pyrochlores (A = Y, Pr-Lu) [4]. In the pyrochlore structure, the Ir^{4+} cations are placed in a geometrically frustrated tetrahedral network and interact through f-d exchange with rare-earth cations. This leads to various emergent phenomena, including, e.g., Weyl semimetal [5] and fragmented spin ice with monopole-like excitations [6]. Synthesis of new iridates is warranted to further the understanding of the Ir^{4+} $j_{eff} = 1/2$ state.

The present work focusses on the magnetic and structural properties of newly synthesised quaternary neodymium iridate single crystals. The present compound displays a crystal structure reminiscent of the ternary pyrochlore $Nd_2Ir_2O_7$ [7], with crucial differences attributed to the Pb-based synthesis method. The crystal structure found using X-ray diffraction is analysed and compared to the pyrochlore structure, with a focus on the Ir pyrochlore-type tetrahedral sublattices with octahedral O^{2-} environments found in both crystal lattices. The full crystal structure contains two Ir sublattices, three Nd sublattices and one Pb sublattice with a high degree of disorder in the form of vacancies. Magnetic properties, including two magnetic transitions at 41 K and 8 K, demonstrate notable similarities for the two crystal variants. The magnetic structure, fundamentally tied to the tetrahedral lattice in the pyrochlore case, is examined in the non-pyrochlore samples employing neutron diffraction.

1. J. G. Rau, E. K.-H. Lee, H.-Y. Kee, *Annu. Rev. Condens. Matter*, **7** (2016) 195-221.
2. K. S. Pedersen, J. Bendix, A. Tressaud, E. Durand, H. Weihe, Z. Salman, T. J. Morsing, D. N. Woodruff, Y. Lan, W. Wernsdorfer, C. Mathoničre, S. Piligkos, S. I. Klokishner, S. Ostrovsky, K. Ollefs, F. Wilhelm, A. Rogalev, R. Clérac, *Nat. Commun.*, **7**, (2016), 12195.
3 C. Lu, J.-M. Liu, *Adv. Mater.*, **32**, (2020), 1904508.
4. W. Witczak-Krempa, G. Chen, Y. B. Kim, L. Balents, *Annu. Rev. Condens. Matter*, **5**, (2014), 57-82.
5. X. Liu, S. Fang, Y. Fu, W. Ge, M. Kareev, J.-W. Kim, Y. Choi, E. Karapetrova, Q. Zhang, L. Gu, E.-S. Choi, F. Wen, J. H.Wilson, G. Fabbris, P. J. Ryan, J. W. Freeland, D. Haskel, W. Wu, J. H. Pixley, J. Chakhalian, *Phys. Rev. Lett.*, **127**, (2021), 277204.
6. E. Lefrançois, V. Cathelin, E. Lhotel, J. Robert, P. Lejay, C. V. Colin, B. Canals, F. Damay, J. Ollivier, B. FÍk, L. C. Chapon, R. Ballou, V. Simonet, *Nat. Commun.*, **8**, (2017), 209.
7. H. Takatsu, K. Watanabe, K. Goto, H. Kadowaki, *Phys. Rev. B* **90**, (2014), 235110.

Student symposium, session II, May 26, Tuesday

SL5

THE EFFECT OF THERMAL ANNEALING ON THE STRUCTURE OF ORGANIC SEMICONDUCTOR THIN FILMS AND POWDERS

J. Čekal, A.F.B. Melécot, D. Varshney and J. Novák

Department of Condensed Matter Physics, Faculty of Science, Masaryk University
Kotlárská 267/2, 611 37 Brno
547890@mail.muni.cz

Organic semiconductors are a relatively new type of material used in applications such as organic solar cells, organic field-effect transistors, and OLED displays. Understanding their thin-film behaviour at elevated temperatures is crucial for the designing of these devices. In this work, we focus on the behaviour of thin films and powders of 2, 3, 6, 7, 10, 11-Hexamethoxytriphenylene (HMTP) and 1, 4, 5, 8, 9, 11-Hexaazatriphenylenehexacarbonitrile (HATCN) molecules during thermal annealing. The main goal of this work was to study phase transitions and the temperature dependence of lattice parameters, focusing on anisotropic behaviour and a potential difference between thin film and powder material. We used in-situ X-ray diffraction (XRD) during annealing to address the material properties. Additionally, we compare reliability and efficiency of three data-fitting methods for the determination of the lattice parameters.

HMTP and HATCN are organic semiconductors with a hexagonal crystal structure. In the HMTP crystal, molecules form a brickwork arrangement. The methoxy groups of one molecule fit into the empty space between the aromatic nuclei of the molecules lying in the planes above and below. This minimises steric hindrance and repulsion between aromatic rings. The lattice parameters of HMTP crystals are reported as 13.1240(13) Å and 6.8481(7) Å in the *a* and *c* directions, respectively [1]. In contrast, the arrangement of HATCN molecules in the crystal is more complicated. The molecules form ladder-like chains. The overall crystal arrangement is governed by perpendicular interactions between the electrons of the heterocycle and the cyano group of the neighbouring molecule. This results in a 3D hexagonal arrangement in the crystal. The reported lattice parameters are 23.537(3) Å and 14.834(3) Å in the *a* and *c* directions, respectively [2].

The HMTP film was prepared using molecular beam epitaxy on a graphene substrate coated on 4H-SiC. The HATCN film was prepared by the drop-coating method from an acetone solution.

Due to the different crystal preferential orientations of the samples, various XRD techniques were used. For powder diffraction measurements (PXRD), we used a symmetric scan employing beam collimated by pinholes and a 2D detector. It was sufficient to use the symmetric out-of-plane scan to probe strong HMTP 0002 reflection for the HMTP film. On the other hand, for the HATCN film, the signal was weak in the out-of-plane direction film. Therefore, we used an in-plane scan in the grazing incidence X-ray diffraction (GIXRD) geometry in this case. All measurements were performed using a Rigaku SmartLab 3 diffractometer equipped with a 9 kW Cu rotation anode. The *in-situ* annealing experiments in the temperature range 30 °C to 140 °C were performed in nitrogen protection atmosphere using a DHS 1100 annealing chamber by Anton Paar GmbH. HMTP and HATCN powders were enclosed in Kapton capsules to avoid material displacement during air suction and nitrogen flushing in the annealing chamber.

As for data processing, we compare reliability and efficiency of the Rietveld, Le Bail, and Cohen methods [3] to obtain lattice parameters temperature dependency out of collected XRD data. For the Rietveld method, which requires a correct structure model, we assumed fixed internal

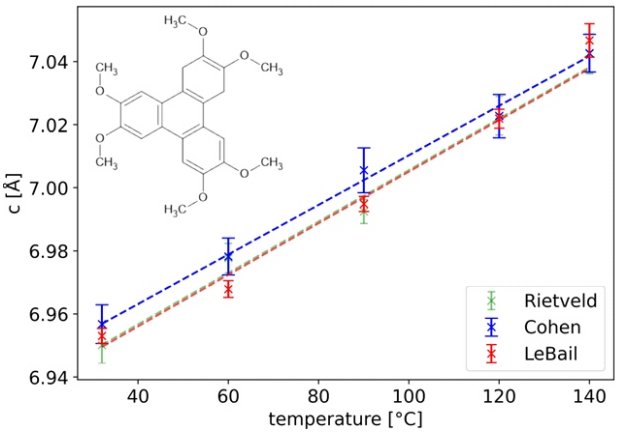

Figure 1. Values of *c* lattice parametres for HMTP powder.

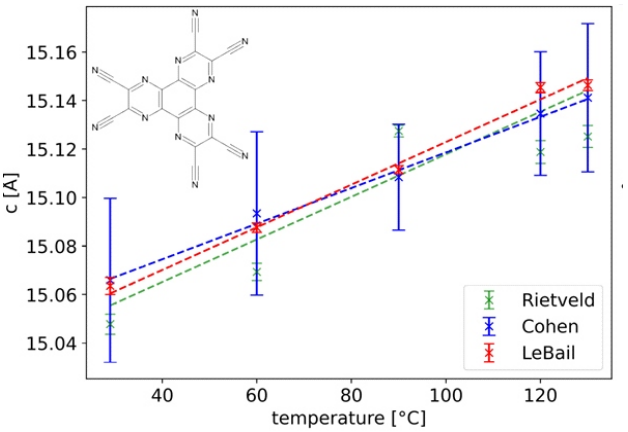

Figure 2. Values of c lattice parametres for HATCN powder.

Table 1. Table of calculated CLTE in *a* and *c* crystal directions for HMTP and HATCN films and powders obtained by different fit methods.

Sample	Fitting method	$_a$ [10^{-5} K^{-1}]	$_c$ [10^{-5} K^{-1}]	Mean ^{2}
HMTP- film	-	-	12.68 ± 0.16	-
HMTP-powder	Cohen	-0.5 ± 0.9	11.3 ± 1.0	-
	Rietvield	0.3 ± 9.2	11.8 ± 1.0	23.82
	Le Bail	0.3 ± 0.5	11.8 ± 0.5	10.73
HATCN- powder	Cohen	3.8 ± 2.4	4.9 ± 2.5	-
	Rietvield	3.7 ± 0.4	5.8 ± 0.3	4.74
	Le Bail	4.0 ± 0.2	5.9 ± 0.2	2.04
HATCN- film	Rietvield	5.5 ± 1.9	5.7 ± 1.7	2.49
	Le Bail	6.1 ± 0.7	6.9 ± 0.9	1.51

structure of the unit cell as obtained from a Crystallographic Information File. For the Le Bail method, which only requires the space group and initial lattice parameters as an input, peak intensities are treated as free parameters. We used implementation of the Rietveld and Le Bail methods in the FullProf programs package [4]. The Cohen method, which depends on a correct peak indexation only but requires absence of overlapping peaks, was used to verify the results of the other two methods. The anisotropic coefficients of linear thermal expansion (CLTE) (1) were calculated from the lattice parameters temperature dependences.

$$\frac{1}{a_{i0}} \quad \frac{a_i}{T} \qquad (1)$$

where a_i is lattice parameter and T is temperature. The dependences of lattice coefficient c for powders of HMTP and HATCN are shown in Fig. 1 and Fig. 2, respectively.

The CLTE values obtained from lattice parameters calculated by the different methods are relatively close with overlapping confidence intervals (Tab. 1). The Cohen method showed lower accuracy for our data, which is noticeable in Fig. 2. Although modeling of the crystal preferential orientation was applied in the Rietveld method , the Le Bail whole-pattern decomposition proved to be the most robust and precise method for our specific goal of extracting lattice parameters, yielding the lowest uncertainties and ignoring complex intensity variations [3].

We found that neither the structural model nor the usage of the specific space group provided a good fit for the HMTP powder data which is indicated by indicated by the high mean ^{2} values in Tab. 1. Additionally, we observed a large thermal expansion anisotropy in the CLTE for the HMTP powder, along with an indication of negative thermal expansion (NTE). According to recent research, the phenomenon of NTE in organic crystals is not as rare as previously assumed [5]. This behaviour in HMTP crystals likely originates from strong intermolecular hydrogen bonds parallel to the crystallographic *a*-axis, contrasted by much weaker interactions along the *c*-axis, perpendicular to the molecular plane. The CLTE of the HMTP film is slightly higher than that of the powder, likely due to interactions with the substrate. For HATCN, the CLTE along the c-direction is nearly identical for both the powder and the film; however, along the a-direction, the film exhibits a value approximately 50% higher than the powder.

1. T. L. Andresen, F. C. Krebs, N. Thorup, K. Bechgaard, *Chem. Mater.*, **12**, (2000), 2428.
2. P. S. Szalay, J. R. Galán-Mascarós, R. Clérac, K. R. Dunbar, *Synth. Met.*, **122**, (2001), 535.
3. V. K. Pecharsky, P. Y. Zavalij, *Fundamentals of Powder Diffraction and Structural Characterization of Materials, Second Edition*. New York: Springer. 2009.
4. J. Rodríguez-Carvajal, FullProf Suite Manual, Version 8.20. Grenoble: Institut Laue-Langevin. 2025.
5. A. van der Lee, D. G. Dumitrescu, *Chem. Sci.*, **12**, (2021), 8537.

CzechNanoLab Research Infrastructure (ID 90251), funded by MEYS CR, is gratefully acknowledged for the financial support of the measurements/sample fabrication.

SL6

SUBSTRATE-CONTROLLED CRYSTALLIZATION AND CRYSTAL ORIENTATION OF HMTP ORGANIC SEMICONDUCTOR THIN FILMS ON GRAPHENE/SiC

Devanshu Varshney,[1] Pavel Procházka,[2] Veronika Stará,[2] Mykhailo Shestopalov,[3] Jan Kunc[3], Jan Čechal[2,4] , Jiří Novák[1]

[1]*Department of Condensed Matter Physics, Faculty of Science, Masaryk University, Kotlářská 2, 61137 Brno, Czech Republic*

[2]*CEITEC - Central European Institute of Technology, Brno University of Technology, Purkyňova 123, 612 00 Brno, Czech Republic.*

[3]*Charles University, Faculty of Mathematics and Physics, Institute of Physics, Ke Karlovu 5, 121 16, Prague 2, Czech Republic*

[4]*Institute of Physical Engineering, Brno University of Technology, Technická 2896/2, 616 69 Brno, Czech Republic.*

We investigate thin films of the -conjugated electron-donor organic semiconductor molecule 2,3,6,7,10,11-hexamethoxytriphenylene (HMTP) on two structurally similar surfaces: single-layer graphene (SLG) on SiC(0001) and the buffer layer on SiC(0001) [1]. Epitaxial graphene on SiC consists of an sp^2-hybridized single-layer graphene above a carbon buffer layer. Although the buffer layer retains a graphene-like lattice, it is partially sp^3-bonded to the underlying Si atoms of the SiC substrate, creating a locally inhomogeneous surface at the nanoscale [2]. In this talk, I will show how these two structurally similar surfaces control both the crystallization and the crystal orientation of HMTP organic semiconductor thin films from the earliest stages of growth.

We combine low-energy electron microscopy and diffraction (LEEM/LEED), which probe the initial growth, with a set of X-ray diffraction techniques, pole figure measurements, azimuthal scans, symmetric scans, and rocking curve measurements, to characterize the crystallographic texture and crystal quality of films up to approximately 30 nm thickness on both surfaces. On SLG, pole figures measured for HMTP $\{10\bar{1}1\}$ reflections reveal two sets of six sharp diffraction spots, confirming highly ordered epitaxial growth with two mirror domains rotated by ±19.1° relative to the graphene lattice (Fig.1(a)). Azimuthal scans show narrow peaks with a full width at half maximum of 0.5°, close to the instrumental resolution, demonstrating exceptional in-plane orientational order. Symmetric scans further reveal that the HMTP {0001} lattice planes are parallel to the sample surface, while the presence of Laue oscillations confirms uniform film thickness and high crystalline coherence.

In contrast, HMTP films grown on the buffer layer exhibit a ring-shaped band of enhanced intensity with slight azimuthal modulation in the pole figure measured for the HMTP $\{10\bar{1}1\}$ reflections (fig.1(b)). The corresponding azimuthal scans show maxima that are approximately 20 times weaker and significantly broader than those observed on SLG, accompanied by a higher continuous intensity profile between the maxima. This indicates a large fraction of randomly oriented crystalline domains. During the initial growth stages, HMTP grows amorphously; however, with increasing film thickness, it evolves into a polycrystalline film with only weak orientational order with respect to the substrate. Furthermore, symmetric scans show that the HMTP {0001} lattice planes are parallel to the sample surface, as observed for HMTP on SLG. However, the absence of Laue oscillations and the lower peak intensity signify reduced crystalline quality.

Finally, we decouple the buffer layer via hydrogen intercalation, which breaks the Si–C bonds and converts the buffer layer into quasi-freestanding graphene [3]. Subsequent growth of HMTP on this surface leads to

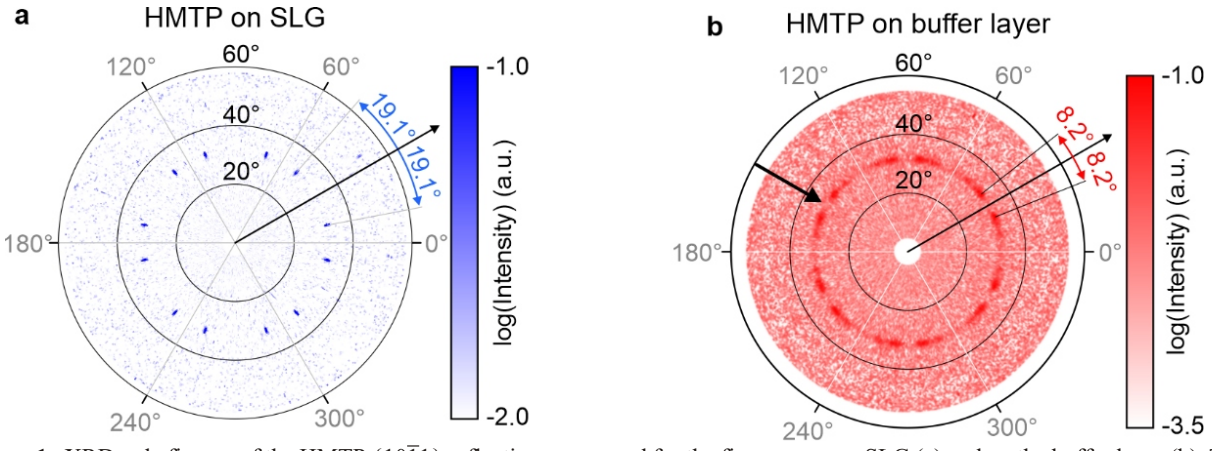

Figure 1. XRD pole figures of the HMTP $\{10\bar{1}1\}$ reflections measured for the fims grown on SLG (a) and on the buffer layer (b). The sharp diffraction spots in (a) and the ring-shaped band of enhanced intensity in (b), indicated by the arrow, are both located at a polar angle of 31.7° with respect to the HMTP [0001] direction.

epitaxial films, demonstrating that the unevenly distributed covalent Si–C bonding between the buffer layer and the SiC substrate is the decisive factor limiting organic semiconductor thin-film crystallinity on graphene/SiC.

1. Varshney, D.; Procházka, P.; Stará, V.; et al. Interfacial Coupling Controls Molecular Epitaxy of HMTP on Graphene/SiC. *ACS Applied Materials & Interfaces* **2026**.
2. Backes, C.; Abdelkader, A. M.; Alonso, C.; et al. Production and Processing of Graphene and Related Materials. *2D Mater.* **2020**, *7*, 022001.
3. Kunc, J.; Rejhon, M.; Hlídek, P.; et al. Hydrogen Intercalation of Epitaxial Graphene and Buffer Layer Probed by Mid-Infrared Absorption and Raman Spectroscopy. *AIP Adv.* **2018**, *8*, 045015.

SL7

XRDlicious: RECENT DEVELOPMENTS IN AN INTERACTIVE PLATFORM FOR POWDER XRD AND STRUCTURAL ANALYSIS

Miroslav Lebeda[1, 2, 3], Jan Drahokoupil[1, 3], Petr Veřtát[1], Petr Vlčák[3]

[1]*FZU – Institute of Physics of the Czech Academy of Sciences*
[2]*Faculty of Nuclear Sciences and Physical Engineering, Czech Technical University in Prague*
[3]*Faculty of Mechanical Engineering, Czech Technical University in Prague*
lebedmi2@cvut.cz

Over the past year, we have developed *XRDlicious*, an interactive application primarily intended for rapid calculation and comparison of theoretical powder X-ray diffraction (XRD) patterns and partial radial distribution functions (see Fig. 1 for an illustration of the interface). We now report on its development, recent improvements, and usage metrics. Among the main additional functionalities are: (1) an integrated search of the MP, MC3D, and COD databases via their public APIs, allowing users to easily retrieve and work with crystal structures directly within the interface; (2) structure visualization and modifications (e.g., atomic species, occupancies, or lattice parameters) to explore their influence on the resulting diffractograms; and (3) convenient conversion between common file types (.xrdml, .ras, and .xy), improving compatibility across various data formats. Developed using Streamlit, the application is also available online (https://xrdlicious.com) and is designed with an emphasis on accessibility and ease of use.

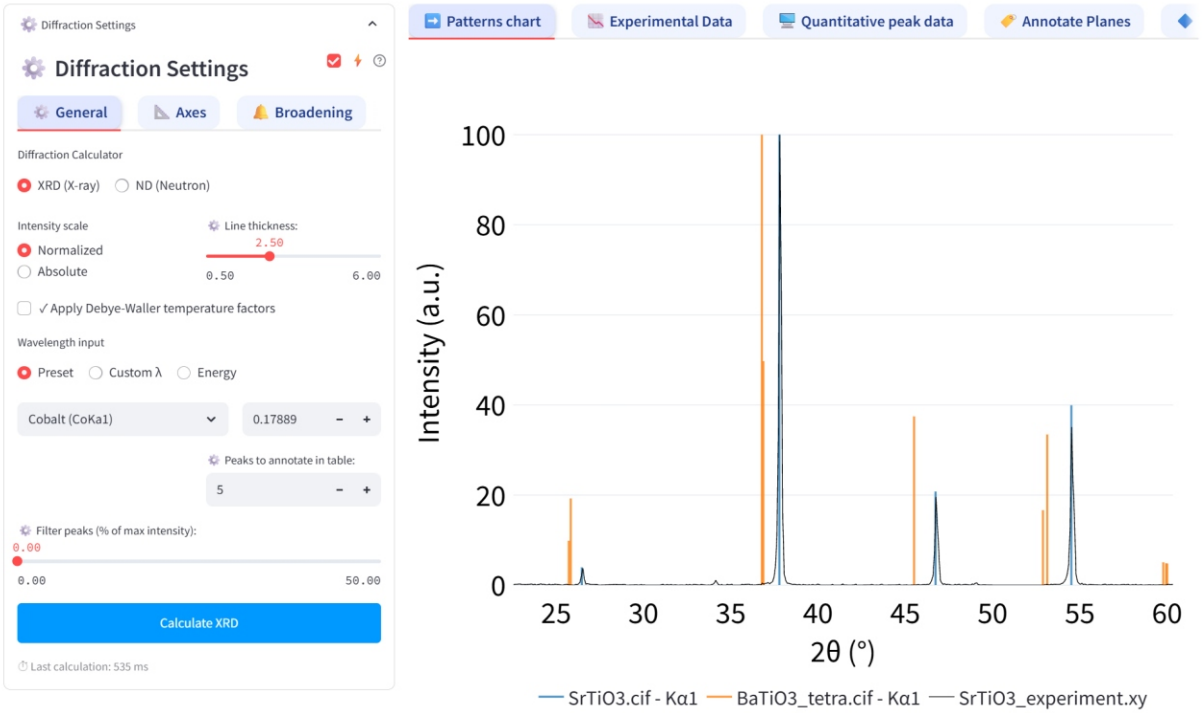

Figure 1. *XRDlicious* interface for calculation and comparison of powder XRD patterns.

SL8

COMPARISON OF PERFORMANCE OF UNIVERSAL MACHINE LEARNING INTERATOMIC POTENTIALS

Z. Holman[1], M. Khanore[1], A. Klic[1], J. Hlinka[1], J. Drahokoupil[1], P. Marton[1]

[1]*Institute of Physics of the Czech Academy of Sciences, Prague, Czech Republic*
[2]*Institute of Mechatronics and Computer Engineering, Technical University of Liberec, Czech Republic*
holman@fzu.cz

Perovskites are materials with the crystal structure ABX_3 that can contain many different cations and anions. This flexibility allows their structural, electrical, and optical properties to be tuned and makes them important for a wide range of applications.

Understanding and improving their properties relies on computational modelling. Density Functional Theory (DFT) is commonly used as a reference method, but it is computationally expensive. Therefore, simplified approaches such as atomistic models, shell models, effective Hamiltonians, and phase-field methods are often used to study larger systems and processes like domain evolution and phase transitions. These models need parameters obtained either from experiments or from first-principles calculations. Recently, machine-learning interatomic potentials (MLIPs) have become a useful alternative because they can reach near-DFT accuracy while allowing relatively large and longe simulations of perovskite oxides.

In this work we evaluate several variants of universal machine-learning interatomic potentials (uMLIP) [1, 2, 3, 4]. We compare their accuracy of energy and forces predictions with DFT calculations. In this work we focused on performance of MACE, PET-MAD uMLIP.

Acknowledgements: The research was supported by Czech Science Foundation Grant No. 24-11275S.

1. Ilyes Batatia, Dávid Péter Kovács, Gregor N. C. Simm, Christoph Ortner, and Gábor Csányi. Mace: Higher order equivariant message passing neural networks for fast and accurate force fields, 2023.

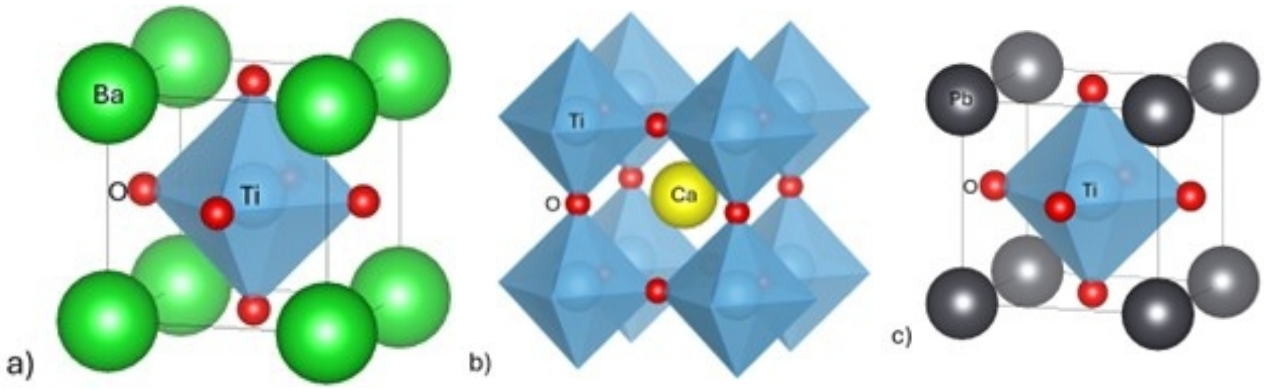

Figure 1. Structures of simulated perovskites a) $BaTiO_3$ b) $CaTiO_3$ c) $PbTiO_3$

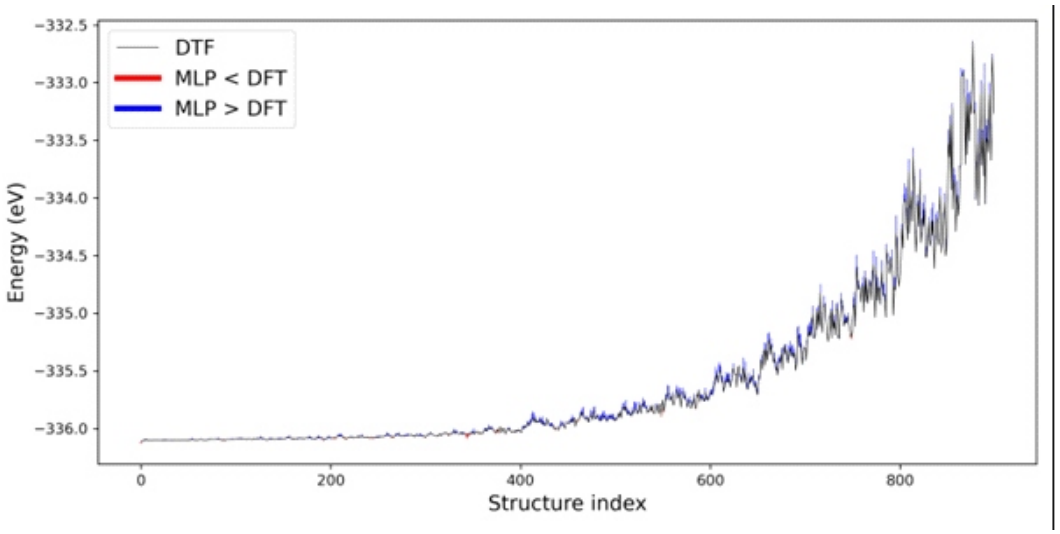

Figure 2. Energy difference between DFT and PET-MAD uMLIP per structure.

2. Dávid Péter Kovács, Ilyes Batatia, Eszter Sára Arany, and Gábor Csányi. Evaluation of the mace force field architecture: From medicinal chemistry to materials science. The Journal of Chemical Physics, 159(4), 2023.
3. Arslan Mazitov, Filippo Bigi, Matthias Kellner, Paolo Pegolo, Davide Tisi, Guillaume Fraux, Sergey Pozdnyakov, Philip Loche, and Michele Ceriotti. Pet-mad, a lightweight universal interatomic potential for advanced materials modeling, 2025.
4. Cesare Malosso, Filippo Bigi, Paolo Pegolo, Joseph W. Abbott, Philip Loche, Mariana Rossi, Michele Ceriotti, and Arslan Mazitov. High-quality, high-information datasets for universal atomistic machine learning, 2026.

Student symposium, session III, May 26, Tuesday

SL9

CRYSTAL STRUCTURE VALIDATION WITH THE USE OF THE DFT METHOD

F. Fňukal

University of Chemistry and Technology, Prague, Technická 5, 166 28 Praha 6 – Dejvice
fnukalf@vscht.cz

Introduction

Current crystal structure validation procedures rely primarily on diffraction data analysis, as implemented in tools such as PLATON/checkCIF [1]. A complementary approach – comparison of the geometry of experimental structures with their DFT-optimized geometries – was introduced by van de Streek & Neumann [2, 3], but did not gain widespread adoption due to high computational demands and reliance on commercial software. Recent advances in computing power and DFT methodology now make this approach practically viable for routine use on standard desktop hardware even for organic molecular crystals with large unit cells.

Method

To facilitate practical application of this approach, we implemented the validation workflow in the program checkCIF-DFT, a freely available program that automates parsing CIF files, management of DFT geometry optimizations via the use of external DFT programs and evaluation of structural discrepancies using a set of comparison descriptors. In our testing so far, geometry optimizations were performed using CASTEP [4] with the r2SCAN [5] meta-GGA functional and Many-Body Dispersion (MBD) correction [6]. Our descriptor set extends the previously proposed r.m.s. Cartesian displacement (RMSCD) [2, 3] with maximum changes in bond lengths, bond angles and torsion angles, maximum Cartesian displacement and a temperature-corrected volume difference – the latter accounting for the formal 0 K conditions of DFT optimization using thermal expansion coefficients derived from Cambridge Structural Database (CSD) [7] data [8].

Results

To set reference values of comparison descriptors, the method was benchmarked against two reference sets: five structures determined by neutron diffraction, representing correct high-quality experimental determinations, and five incorrect structures known to be obtained by data manipulation and fraud [9]. The use of our extended comparison descriptor set is justified as the use of the original RMSCD criterion fails to flag three of the five fraudulent structures as problematic, which was already noted by van de Streek & Neumann in their work. However, the extended comparison descriptor set – particularly maximum bond length difference and maximum bond angle difference – clearly separated all five fraudulent structures from the neutron structures supporting the idea of the need for a multi-parameter validation approach.

The validation procedure was next applied to a representative set of 100 organic crystal structures drawn from the CSD. Of these, 90 calculations completed and the large majority showed deviations consistent with correct experimental determinations (see Fig. 1). However, a subset showed elevated deviations revealing several recurring categories of structural problems: unmodelled solvent-accessible voids, missing atoms, incorrect space group assignment etc. Notably, several calculation failures were also associated with structures showing some of these problems, which offers a possible explanation to the calculation difficulties.

Conclusions

Our results suggest that DFT-based crystal structure validation may serve as a physically grounded complementary validation method to conventional validation checks. This independent validation is of great use especially in cases where determination errors were made but are difficult to spot or in cases where determination details are poorly documented. Furthermore, the results suggest that the CSD is not free of structures with serious structural issues, even among those that have passed conventional validation filters. Our implementation of the method – the program checkCIF-DFT – is planned to be made freely available and is intended to make this DFT validation workflow accessible to the broad crystallographic community. Additionally, it is planned to extend checkCIF-DFT with pre-calculation checks to reveal most common structural issues that are identifiable prior to DFT optimization calculations. Furthermore, support for the use of Machine Learning Interatomic Potentials (MLIPs) is being developed as a significantly faster alternative to DFT calculations.

1. A. L. Spek, Acta Cryst., D65, (2009), 148.